In Situ Temperature Measurements at the Svalbard Continental Margin: Implications for Gas Hydrate Dynamics

M. Riedel[1] [ID], **K. Wallmann[1], C. Berndt[1]** [ID]**, T. Pape[2,3]** [ID]**, T. Freudenthal[3], M. Bergenthal[3], S. Bünz[4], and G. Bohrmann[2,3]**

[1]GEOMAR Helmholtz Centre for Ocean Research Kiel, Kiel, Germany, [2]Department of Geosciences, University Bremen, Bremen, Germany, [3]MARUM Center for Marine Environmental Sciences, University Bremen, Bremen, Germany, [4]Centre for Arctic Gas Hydrate, Environment and Climate, Tromsø, Norway

Abstract During expedition MARIA S. MERIAN MSM57/2 to the Svalbard margin offshore Prins Karls Forland, the seafloor drill rig MARUM-MeBo70 was used to assess the landward termination of the gas hydrate system in water depths between 340 and 446 m. The study region shows abundant seafloor gas vents, clustered at a water depth of ∼400 m. The sedimentary environment within the upper 100 m below seafloor (mbsf) is dominated by ice-berg scours and glacial unconformities. Sediments cored included glacial diamictons and sheet-sands interbedded with mud. Seismic data show a bottom simulating reflector terminating ∼30 km seaward in ∼760 m water depth before it reaches the theoretical limit of the gas hydrate stability zone (GHSZ) at the drilling transect. We present results of the first in situ temperature measurements conducted with MeBo70 down to 28 mbsf. The data yield temperature gradients between ∼38°C km^{-1} at the deepest site (446 m) and ∼41°C km^{-1} at a shallower drill site (390 m). These data constrain combined with in situ pore-fluid data, sediment porosities, and thermal conductivities the dynamic evolution of the GHSZ during the past 70 years for which bottom water temperature records exist. Gas hydrate is not stable in the sediments at sites shallower than 390 m water depth at the time of acquisition (August 2016). Only at the drill site in 446 m water depth, favorable gas hydrate stability conditions are met (maximum vertical extent of ∼60 mbsf); however, coring did not encounter any gas hydrates.

1. Introduction

Widespread methane plumes have been observed at the upper western Svalbard continental margin (Figure 1) in the water column between 80 and 415 m water depth (Sahling et al. 2014; Westbrook et al., 2009) revealing a maximum abundance around the 400 m isobath. This accumulation of gas emission sites was initially interpreted by Westbrook et al. (2009) to be the result of gas hydrate dissociation in response to recent bottom water warming, but dating of the associated authigenic carbonates showed that gas seepage at some of these locations had been ongoing for several thousands of years (Berndt et al., 2014).

The R/V MARIA S. MERIAN cruise MSM57/2 in late summer of 2016 was set to collect new data in the region of gas venting off Svalbard to further constrain the interaction of fluid/gas flow from the sediments into the water column, and the gas hydrate dynamics in relation to bottom water temperature changes. It is important to understand how gas hydrate reservoirs will react to future increases in bottom-water temperature, and if such warming may trigger a sudden release of methane leading to accelerated climate warming. Current understanding of Earth's potential future climate predicts an amplification of warming especially for Arctic regions (e.g., Intergovernmental Panel on Climate Change, 2007). Earlier studies about possible feedback mechanisms between methane from gas hydrate reservoirs and climate change have led to the formulation of the clathrate gun hypothesis by Kennett et al. (2003). However, there is considerable uncertainty and debate on how much methane from destabilized gas hydrates may actually reach the atmosphere (see e.g., review by Ruppel & Kessler, 2017). Studies of the feather-edge of gas hydrate stability along the western and eastern US continental margin as well as the US Beaufort Sea suggested ongoing changes to the gas hydrate system from recent bottom water warming (e.g., Hautala et al., 2014; Johnson et al., 2015; Phrampus & Hornbach, 2012; Phrampus et al., 2014), similar to the hypothesis by Westbrook et al. (2009) or Thatcher et al. (2013). However, all these studies lack in situ data on geothermal gradients, sediment thermal conductivity, and presence (or absence) of gas hydrates with depth. Here, we report on the first drilling

and in situ temperature measurements through the shallow feather-edge of the gas hydrate system off Svalbard (Figure 2). We combine the new data from these measurements with sediment-derived porosity and pore-fluid data to develop a better understanding of the dynamic gas hydrate system, model the temporal evolution of gas hydrates along the continental margin and estimate the extent of the current and past gas hydrate stability zone. Data from long-term bottom water temperature changes (Berndt et al., 2014) already suggested a seasonal variability and fast-changing extent of the gas hydrate system. However, these previous studies lacked measurement-based constraints of the deep geothermal gradients.

Geological Setting The western Svalbard margin (Figure 1) is the result of Early Eocene oblique rifting between Eurasia and Greenland as the north Atlantic opened (Eldholm et al. 1987; Faleide et al., 1996). The heterogeneous geomorphology of the area is a result of glacial activity during the Pliocene and Pleistocene transition (Knies et al., 2009; Solheim et al., 1998). During this geological time, the Svalbard-Barents Sea ice-sheet retreated and advanced repeatedly, sometimes reaching the shelf break. The analysis of prograding
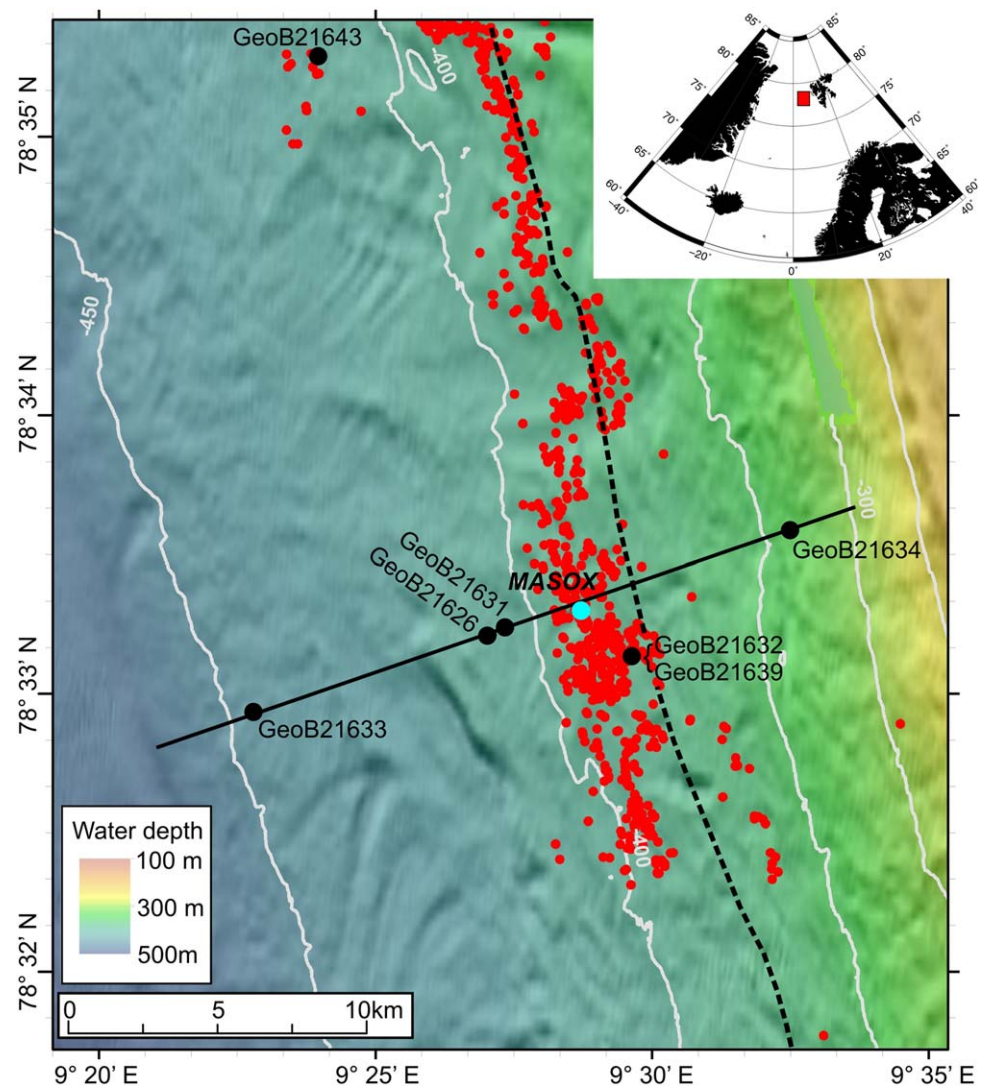
Figure 1. Location of study region in the Fram Strait (inset) and bathymetric map of study region (compiled from numerous cruises, details see Acknowledgments) at the upper continental margin slope west of Prins Karls Forland. MeBo drill holes at six sites occupied during MSM57 are shown as black dots (see Table 1 for details). Gas emission sites (red circles) were taken from Sahling et al. (2014). Solid black line is location of seismic data shown in Figure 2. Blue dot indicates location of the long-term observatory site MASOX (Berndt et al., 2014). The black dashed line is the approximate location of the theoretical maximum extent of the sI gas hydrate stability zone as constrained from the temperature data and modelling applied for the time of the MSM57 expedition (see Table 2 for details).
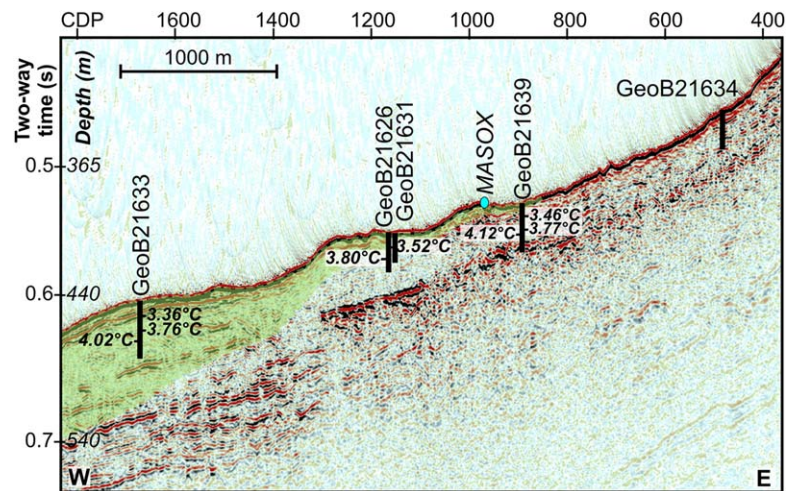
Figure 2. Section of a 2-D seismic line (CAGE14-HR2D-04) acquired with a 100m long streamer and 2 GI guns along the drilling transect. Details on seismic processing of this line are found in Plaza-Faverola et al. (2017). All drill sites are indicated by black lines with lengths of bars corresponding to penetration depths. Temperature measurements are shown by labels. The green-shaded polygon outlines the theoretically maximum possible region of stable sI gas hydrate at the time of expedition MSM57 using the new temperature data (August 2016) and modelling applied (see Table 2 for details). Blue dot corresponds to the MASOX observatory (Berndt et al., 2014).

glacigenic sequences suggests that major glacier advances at the Svalbard continental margin happened at peak glaciations during the last 3.2 million years (Landvik et al. 1998; Rajan et al. 2012; Sarkar et al. 2012). The shelf break marks the approximate maximum extent of the ice coverage (Landvik et al., 2005). The shelf was flooded as glacial ice retreated approximately 13,000 years ago. Sub-sea geomorphological features have been characterized and reported e.g., by Vanneste et al. (2007), Rajan et al. (2012), and Sarkar et al. (2012), and include abundant, moraine ridges, ice-berg scours and circular to elliptical crater-like depressions (kettle-lake terrain) from isolated and stranded ice-bergs. Furthermore, negative-polarity bright spots in seismic data, zones of low acoustic velocity combined with high seismic attenuation suggest free gas accumulations below seafloor seeps (Ker et al., 2014; Sarkar et al., 2012).

2. Data and Methods

The sea floor drill rig MARUM-MeBo70 was used for getting core samples of unconsolidated sediments and for conducting formation temperature measurements. A detailed description of this robotic drilling device is given in Freudenthal and Wefer (2013). Sediment core samples were drilled with a wire line coring technique and a core diameter of 55 mm. Stroke length per core barrel typically was 2.35–2.5 m.

As the sediments consist of diamictons with large rock pieces of ice-rafted debris and hemipelagic sediments the geological conditions for drilling offshore Svalbard are challenging. Still, we reached a maximum drilling depth of 38 m.

2.1. Temperature Measurements With MeBo70

Core drilling was interrupted at distinct depths for conducting in situ temperature measurements in the MeBo bore holes using a miniature temperature data logger (MTL) built by 'Antares' (type 1854). The MTL was mounted into a cone tip pilot (Figure 3a), that penetrates through the core drilling bit at the bottom end of the drill string. The electronics and battery of the MTL are located in a 16 mm housing above a 100 mm-long stainless steel tube with a diameter of 5 mm. The MTL records data every 3 s for a total of 48 h. Data acquisition is autonomous inside the MTL for the duration of deployment. After recovery, the temperature data were downloaded from the MTL including a time-stamp, raw resistivity value, and converted values of temperature. At pre-defined drilling-depths, the MTL was inserted by about 10 to 15 cm into the sediment, resulting in a frictional heating pulse (Figure 3b) that then decays over time. The probe was left in the sediments for up to 10 minutes, and temperatures may reach equilibrium temperature of the
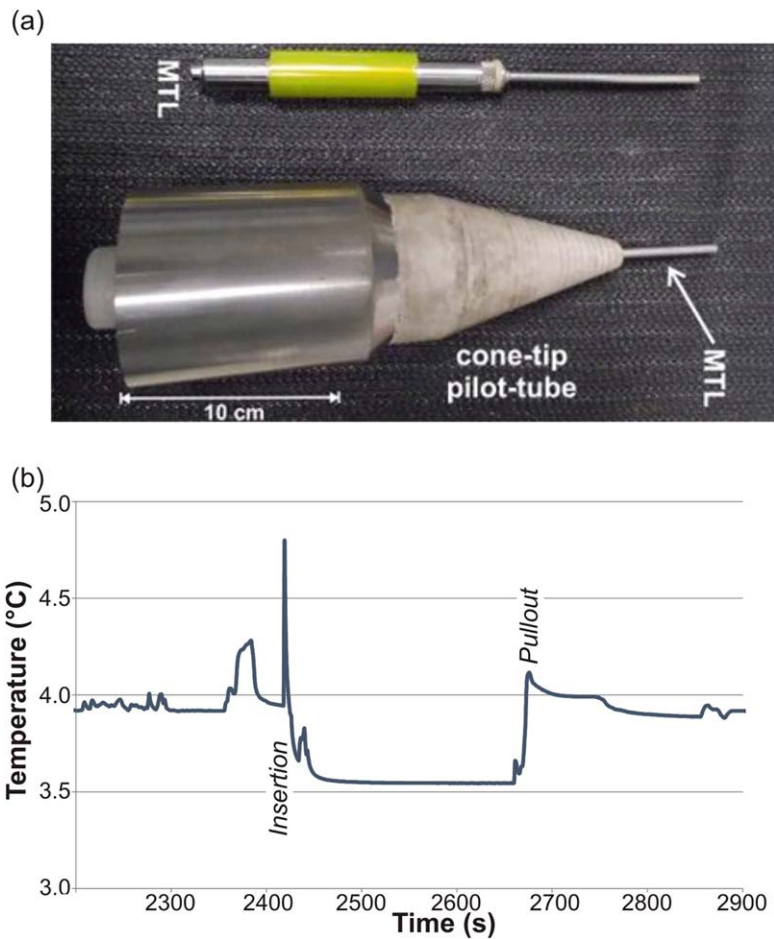
Figure 3. (a) Image of the MTL inside a pilot tube (lower) and the MTL itself (upper). (b) Example of a temperature record from Station GeoB21643-1 at a depth of 12.1 m below seafloor (mbsf). (For calculated sediment temperatures see also Table 1).

Table 1

Stations With MARUM MeBo-70 Temperature Measurements, Depth of Measurement (Meters Below Seafloor, mbsf), and Estimated In Situ Temperatures

Station	Depth (mbsf)	Temperature (°C)	Water depth (m)
GeoB21632-2	10.3	3.46	391
	17.9	3.77	
GeoB21626-1,2	10.33	3.486	404
	10.33	3.546	
	17.93	3.796	
GeoB21631-1	12.82	Not successful	405
GeoB21633-1	10.33	3.353	446
GeoB21633-3	10.33	3.375	446
	20.33	3.758	
	27.93	4.02	
GeoB21634-1	9.88	Not successful	340
GeoB21639-1	12.75	Not successful	391
	21.63	4.119	
GeoB21643-1	12.13	3.565	402
	19.28	3.817	
	26.3	4.366	

formation. However, as this is not necessarily always the case, we used an additional analysis-step to extrapolate the incomplete temperature decay curve to the equilibrium stage using a plot of temperature as function of reciprocal time. A linear fit to this data-curve then yields an estimate of the equilibrium temperature as the intersection of the linear fit at reciprocal time "zero" (i.e., infinity). Table 1 shows all estimated equilibrium in situ temperatures. Prior to the insertion of the temperature tool, the sediment surface at the drill bit experiences some cooling from the borehole being filled with seawater, which has approximately the temperature of the bottom-water. Modelling of this cooling process showed that temperature measurements with the MTLs (conducted typically 1 h after the last core is taken) may yield values up to 1 mK too cold for temperature differences of $\sim$1°C between the true in situ conditions and the bottom water. The drilling-induced disturbance scales with the temperature difference between true in situ condition and bottom water temperature. Overall, the disturbance experienced during our experiment is in the order of the absolute measurement accuracy of the MTLs and therefore deemed negligible in the context of our study.

In total, 16 deployments of the temperature tool were completed during the drilling, out which twelve deployments yielded reliable in situ temperatures. Unsuccessful deployments were encountered mostly due to multiple frictional heat pulses when the probe was not stable within the sediments, so that no useful temperature decay could be observed. The in situ temperatures inferred from the successful tool runs were then used to define thermal gradients. These gradients were estimated without the seafloor temperature (in our case, seafloor temperature were around $3 \pm 0.1°C$ along the drilling transect) as this value is changing seasonally. Thermal conductivities of the near-seafloor sediments were determined in previous experiments (Berndt et al., 2014) and showed values that increase with decreasing water depth. Thermal conductivity values are around 1.7 $Wm^{-1}K^{-1}$ at water depths of 446 m (GeoB21633) and increase to $\sim$2.0 $Wm^{-1}K^{-1}$ at water depths of $\sim$390 m (GeoB21639).

2.2. Porosity-Derived Thermal Conductivity

From the recovered sediments, sub-samples with a constant volume plug were taken to measure porosity. The plugs (including the lid) were weighed before sampling. Sediment samples were taken on board as soon as possible after core recovery to minimize moisture loss. In the laboratory at MARUM, the sediment-filled plugs were weighed with the wet sediment inside, as well as after drying by lyophilization for 24 h. The difference in dry- and wet-weight was then used to define the water content of the sediments. Under the assumptions of constant volume per sample taken, a seawater density of 1,023 kg/m^3 for the pore-fluid, and a grain density of 2,500 kg/m^3 for the average sediment, porosity was calculated from the water content. With these assumptions and simplifications applied, the uncertainty of the porosity values is estimated to be between 5 – 10%, depending on lithology (applicability of a uniform grain density value) and variations in pore-fluid salinity.

Thermal conductivity was measured in situ for near-seafloor sediments with a heat-probe along the MeBo drilling transect (Berndt et al., 2014). Using the porosity values and simplified assumptions on lithology, the combined thermal conductivity λ_{sed} of the deeper sediment is then described in the absence of free gas and gas hydrate (using the expression for the geometric mean as an approximation of the effective thermal conductivity, following the argumentation of Huetter et al. (2008) based on Woodside and Messmer (1961) as:

$$\lambda_{\text{sed}} = \lambda_{\text{solid}}^{(1-\Phi)} \times \lambda_{\text{fluid}}^{\Phi} \tag{1}$$

with λ_{solid} and λ_{fluid} as thermal conductivity of the solid grains (5.0 $Wm^{-1}K^{-1}$) representing a mix of sand and clay with drop stones. We chose those to match the average in situ measurements of thermal conductivity reported in Berndt et al. (2014) and pore-water with sea-water salinity (0.58 $Wm^{-1}K^{-1}$; Castelli et al., 1974; Sharqway et al., 2010), respectively, and porosity Φ. Figure 4 shows the results of the calculation of thermal conductivity from the drilling-derived porosity values in the upper 10 m below seafloor in comparison to the data from the shallow deployments of the temperature probe (Berndt et al., 2014).

2.3. Thermal Modeling Approach

We used the following energy equation to simulate heat flow considering multi-phase conduction:

$$\frac{\partial}{\partial t}(C_V \cdot T) = \frac{\partial}{\partial z}\left(\lambda \cdot \frac{\partial T}{\partial z}\right) \tag{2}$$

where T is temperature, z is depth, t is time, C_V is the volumetric thermal heat capacity of the solid-water mixture and λ is the effective thermal conductivity calculated using equation (1). C_V is defined as:
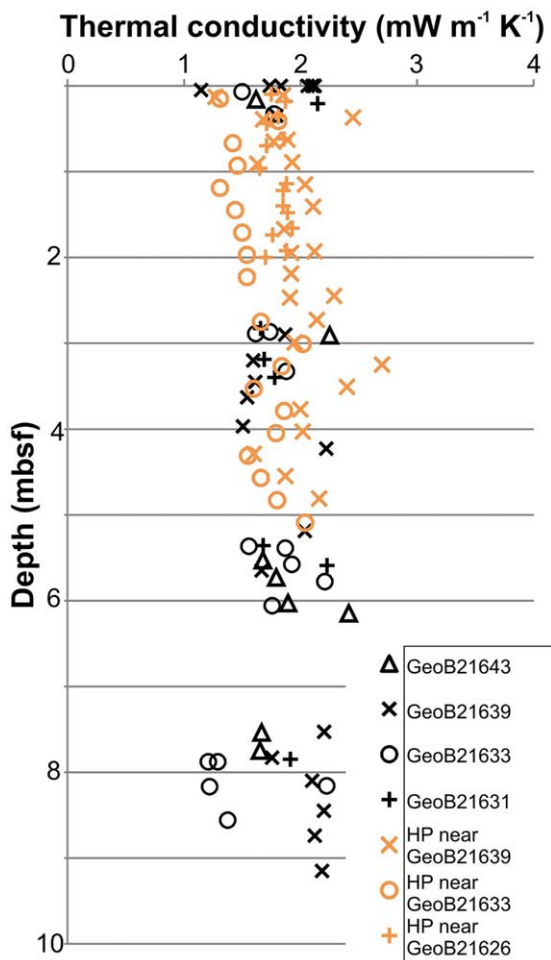
Figure 4. Calculated thermal conductivities using porosity values obtained from MeBo cores (black) within the upper 10 m below seafloor (mbsf) compared with directly measured thermal conductivities using a heat-probe (HP, orange symbols) from Berndt et al. (2014). Site-nomenclature as in Figure 1 and Figure 2; all other site descriptors used in text see Table 1.

$$C_V = (1 - \Phi) \cdot C_S + \Phi \cdot C_W \tag{3}$$

where porosity (Φ) decreases down-core due to compaction while thermal conductivities and heat capacities of the individual phases (s: sediment grains, w: porewater) are assumed to be constant over depth ($C_S = 750$ kJ m^{-3} K^{-1}, $C_W = 4{,}310$ kJ m^{-3} K^{-1}, $\lambda_S = 5$ J m^{-1} K^{-1} s^{-1}, $\lambda_W = 0.58$ J m^{-1} K^{-1} s^{-1}). An exponential function is used to describe the observed decrease in porosity with sediment depth (z):

$$\Phi = (\Phi_i - \Phi_f) \cdot e^{-p \cdot z} + \Phi_f \tag{4}$$

A nonlinear fit through the porosity data yields the following parameter values: $\Phi_i = 0.52 \pm 0.03$, $\Phi_f = 0.39 \pm 0.01$, and $p = 0.12 \pm 0.05$ m^{-1}. Eq. (4) combined with Eqs. (1) and (3) is used to calculate the depth profiles of thermal conductivity and heat capacity (Figure 5) through the entire model-depth.

This model neglects any effect of latent heat from gas hydrate formation or dissociation as well as any advective terms. During expedition MSM57, we did not core gas hydrate at any of the sites visited. Additionally, the regional gradients in pore water sulfate concentration suggest a depth of the sulfate methane reaction zone of 5–6 m below seafloor (mbsf) (see e.g., Graves et al., 2017; Wallmann et al., 2018). These sulfate gradients are balanced by methane fluxes that yield depths of >15 mbsf where methane would exceed the solubility threshold. Thus, the wide-spread gas hydrate formation would only be possible below such depths. This approach does not exclude, however, that there are local accumulations of gas hydrate below the seeps sites, where free gas escapes at the seafloor.

We applied a time-dependent bottom water temperature (T_{BW}) as the upper boundary condition. In August 2016, we registered a stable T_{BW} value of 3.0°C at 390 – 450 m water depth while continuous temperature monitoring at 390 m water depth in 2010–2012 revealed a strong seasonality with minimum temperatures of 2–2.5°C during May–June and maximum temperatures of 3.5 – 4°C during November–December (Berndt et al., 2014). The long-term instrumental record indicates a trend of bottom water cooling from 1945 to 1980 followed by a temperature rise until 2010 (Ferré et al., 2012), where summer temperatures at 400 m water depth increased by about 1°C (Westbrook et al., 2009). The T_{BW} record applied as the upper boundary condition in our thermal model was constructed considering these observations (Figure 6). A constant geothermal heat flux was applied at the base of the model column located at 100 m sediment depth while the steady state solution of the heat equation (Eq. (2)) for $T_{BW} = 3$°C was applied as initial condition. The model was solved numerically over the model period 1945–2016 using finite differences and the method-of-lines approach as implemented in MATHEMATICA's PDE solver. The heat flux applied at the base of the model
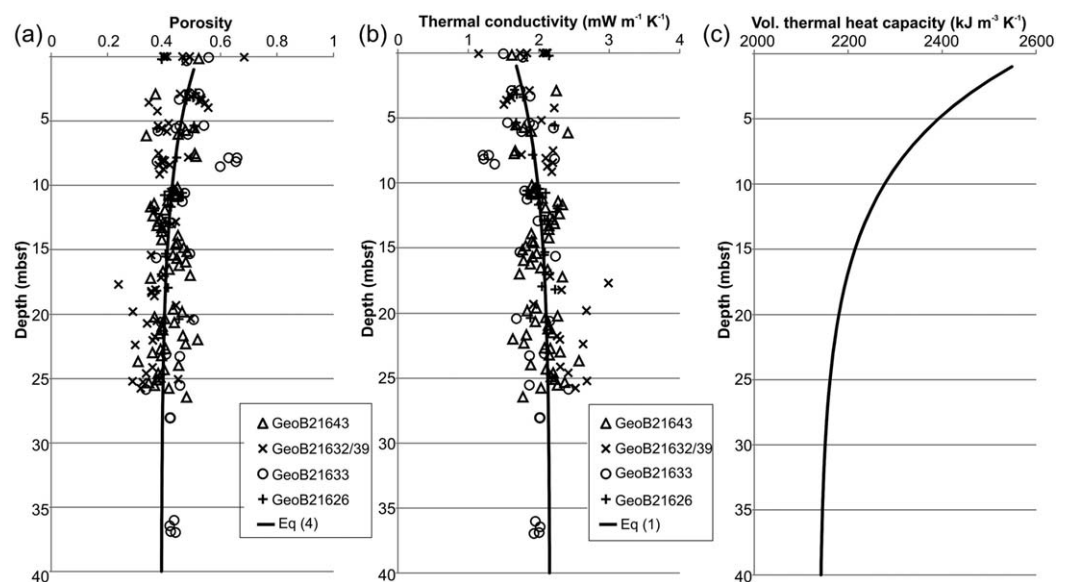
Figure 5. Depth dependent functions based on Eqs (1), (3) and (4) applied in the thermal modeling: (a) porosity from all drill sites and all depths, (b) effective thermal conductivity, and (c) volumetric thermal heat capacity.
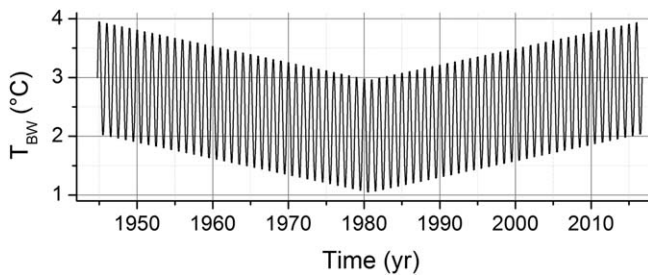
Figure 6. Bottom water temperature (T_{BW}; 1945–2016) applied as upper boundary condition in the thermal modeling.

column was varied in multiple model runs until the model output for the year 2016 was consistent with the sediment temperature data obtained during the cruise.

3 Results

3.1. Temperature Gradients

Four drill sites contain sufficient temperature data at depth to determine thermal gradients (Figure 7). Seafloor temperatures were not used to extrapolate these gradients to shallower depths as the near-seafloor sediments are affected by strong seasonal temperature variations. During the measurements with a heat-probe in late summer 2012 (Berndt et al., 2014), seafloor temperatures were in excess of 4°C, higher than the temperatures determined with MeBo in late summer 2016. Overall, the thermal gradients from the MeBo data are relatively uniform at all sites and estimated values range from $\sim$35°C km^{-1} at Site GeoB21643 to $\sim$41°C km^{-1} at Site GeoB21632/39. Each temperature value is determined with high accuracy (10^{-4}°C) but the gradients do exhibit some uncertainty, partly because data were combined from different boreholes. Here, the uncertainties in the thermal gradients are $\pm$10°C km^{-1} and $\pm$5°C km^{-1}, respectively. No uncertainty was derived for thermal gradients at Sites GeoB21632/39 and GeoB21643, where only two reliable temperature data points exist per drill site.

3.2. Extent of sI Gas Hydrate Stability Zone

The MeBo-derived temperature data define the vertical extent of the theoretical structure 1 (sI) gas hydrate stability boundary at the drill sites. Pore water freshening defined from the MeBo cores shows a decreasing trend with depth and pore water chlorinity is $\sim$6% lower than seawater (which is equivalent to a salinity of 32 PSU). Gas chemistry at all drill sites suggests methane as nearly exclusive hydrocarbon with higher hydrocarbons being present only in traces (Bohrmann et al., 2017; Sahling et al., 2014). Using the phase boundary definition after Tishchenko et al. (2005) and assuming hydrostatic pressure using an average water density of 1,029 kg/m^3 we obtain the theoretical gas hydrate phase boundary shown in Figure 8 (and superimposed on the seismic data seen in Figure 2). The calculations show that only Site GeoB21633 in a water depth of 446 m was inside the gas hydrate stability zone in August 2016. Here, the depth of the base
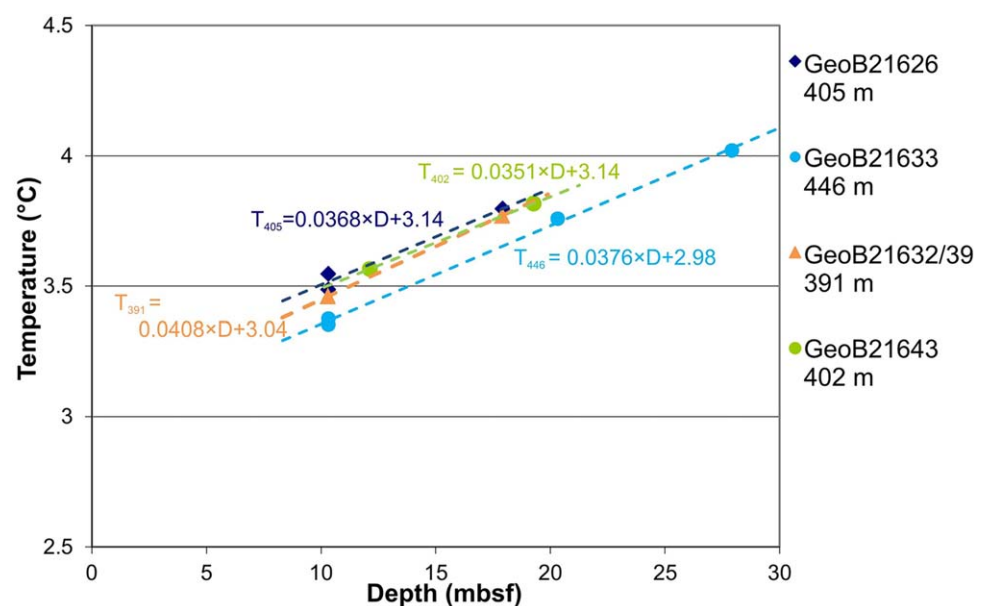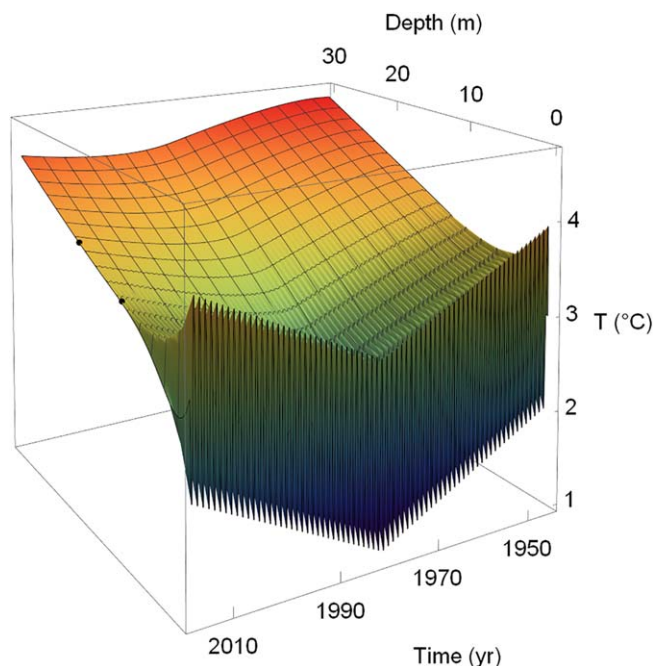

Figure 7. In situ temperature data, linear regression, and inferred temperature gradients for all MeBo sites offshore Prins Karls Forland.
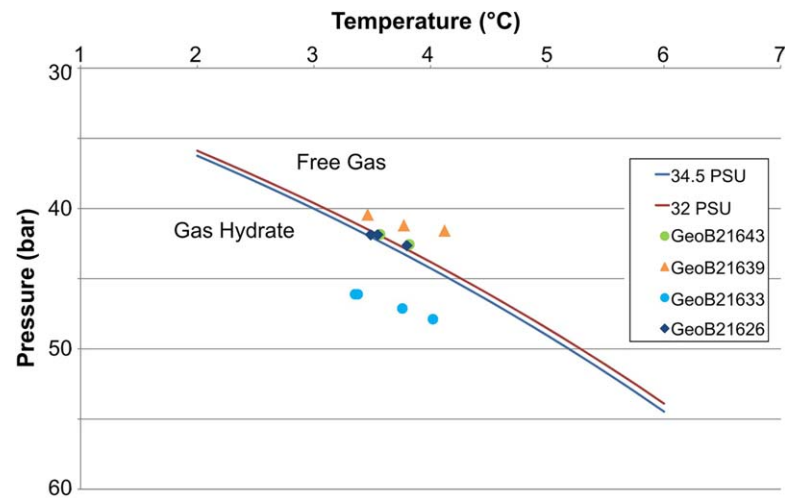
Figure 8. Phase diagram for gas hydrates (sI) using pure methane gas (Tishchenko et al., 2005). Shown are the stability boundaries for two different in situ pore fluid salinities as well as the location of the MeBo temperature data from in situ measurements. Along the transect shown in Figure 2, only data from the drill site in 446 m water depth (GeoB26133) are completely within the gas hydrate stability field. Only temperature and pressure data pairs for successful temperature measurements are shown.

of gas hydrate stability is around 510 m total depth, or equivalent to 65 mbsf. Nevertheless, drilling and coring at this site did not recover any gas hydrates albeit at a core recovery of only ~ 21.5%.

The reflection seismic data along the drilling transect do not show any typical marine bottom-simulating reflector (BSR, Figure 2). A reflection with reversed polarity is associated with an erosional unconformity that shows typical ice-berg scours when traced across the region. Drilling and coring with MeBo recovered a thick uniform sand layer at the depth of this reversed-polarity reflection. We interpret this sand layer as a glacial sand sheet that was deposited proximal to the ice edge during glacial retreat on top of the erosional unconformity into an underlying clay- and silt-rich unit. The presence of this significant change in lithology is likely sufficient for explaining the polarity reversal – although locally, this layer may also be charged with free gas giving rise to the bright-spots seen across the region (Ker et al., 2014).

3.3. Temporal Evolution of Dynamic Extent of sI Gas Hydrate Stability Zone

Figure 9 shows the model results for drill site GeoB21632 at 391 m water depth as an example for all calculations performed at all drilling sites (see Table 2 for all results). The best fit to the temperature observations was obtained applying a basal heat flux of 108 mW·m^{-2} corresponding to a geothermal temperature gradient of 50°C km^{-1} at 100 m sediment depth. Uncertainties in these values are difficult to assess due to the assumptions applied (i.e., starting conditions of the temperature record, Figure 6). Based on the spread in porosity and calculated thermal conductivity values as well as thermal gradients, uncertainty in the obtained deeper thermal gradient unaffected by seasonal and decadal fluctuations is likely in the order of 10%.

The temperature profile obtained with MeBo70 in 2016 reflects the previous cold period and deviates significantly from the steady state profile applied as initial condition (Figure 10). Seasonal T_{BW} changes have a strong effect on the upper 10 m of the sediment column while the decadal T_{BW} variability affects the sediment down to a depth of 80 m. The model was fitted to all temperature data measured at the

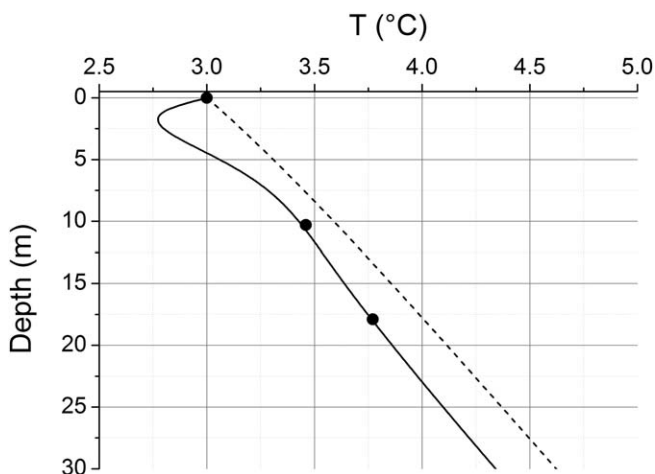**Figure 9.** Results of the thermal modeling for site GeoB21632, a geothermal heat flux of 108 mW·m^{-2} was applied at 100 m sediment depth. Solid black dots indicate the two measurements obtained in August 2016 (see also Figure 7).

Table 2
Model Results for the Gas Hydrate Stability Zone (GHSZ) Using sI Methane Hydrate and a Salinity of 34.5 PSU

Station	Water depth (m)	Heat flow at 100 mbsf (mW × m^{-2})	Temperature gradient at 100 mbsf (°C × km^{-1})	Temperature gradient from Figure 7 (°C × km^{-1})	Base of GHSZ (m) 2016	
					(min)	(max)
GeoB21632-2	391	108	50	40.8	0	4.6
GeoB21639-1	391	123	57	40.8	0	4.2
GeoB21643-1	402	117	54	35.1	1.0	10.0
GeoB21631-1,2	404	112	52	36.8	10.6	12.5
GeoB21633-1	446	93	43	37.6	58.7	58.7
GeoB21633-3	446	95	44	37.6	56.5	56.5

investigated sites applying the same initial conditions. The geothermal heat flow calculated with this non-steady state approach ranges from 93 to 123 mW·m^{-2} and decreases with increasing water depth (Table 2). This observed trend is a local variation and not to be mistaken by the larger (regional) trend in heat flow discussed by Vanneste et al. (2005), which is influenced by the presence of the nearby Knipovich Ridge and Molloy Fracture zone.
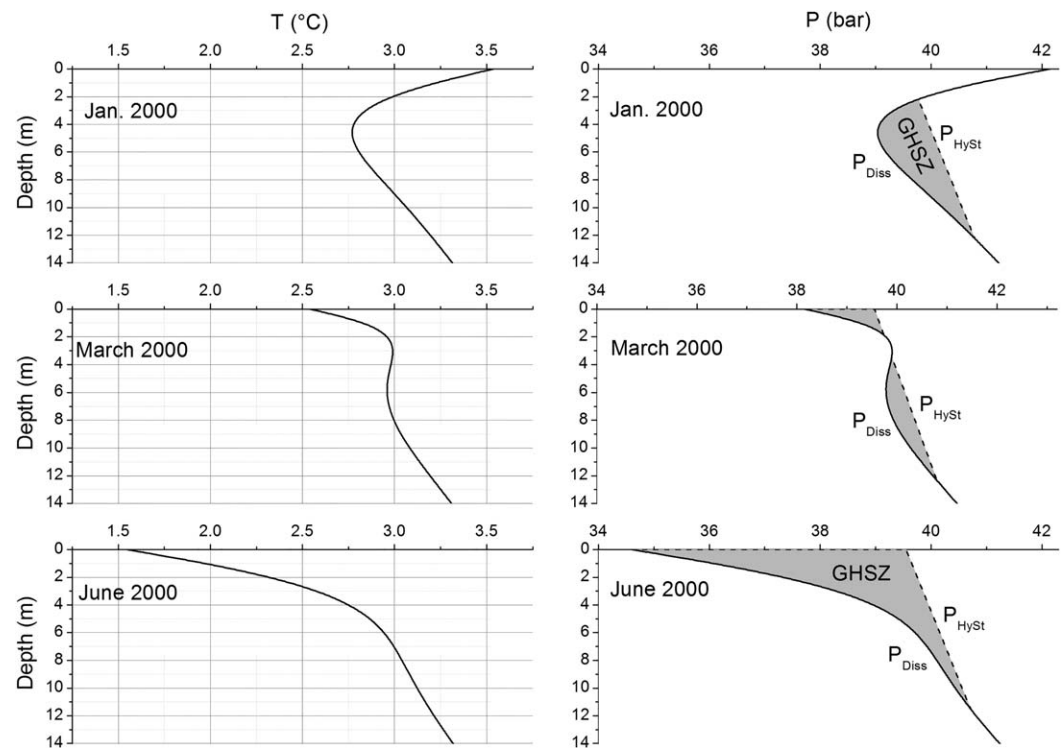
The dissociation pressure of sI gas hydrate (P_{Diss}) was calculated considering ambient sediment temperature and sulfate-free pore water with a salinity of 34.5 PSU (Tishchenko et al., 2005). Hydrostatic pressure (P_{HySt}) was calculated from total depth (water + sediment depth) applying a gravitational constant of 9.83 m s^{-2} (given the latitude of the study sites), and a mean seawater density of 1,029 kg m^{-3}. Methane hydrates are stable where the in-situ pressure (P_{HySt}) exceeds the dissociation pressure (P_{Diss}). According to the thermal model, the strong seasonal change in bottom water temperature affects the stability of gas hydrates in surface sediments. High T_{BW} values during winter inhibit gas hydrate formation in the uppermost layer while gas hydrates are stable during summer when T_{BW} is low (Figure 11). During spring a subsurface temperature maximum may develop that separates the GHSZ in two distinct sublayers. The thickness of the GHSZ (e. g. total thickness of all sediment layers where methane hydrate is stable) varies on seasonal and decadal time scales (Figure 12). It follows the decadal bottom water forcing with a time lag of about 5 years that arises due to the warm initial condition (Figure 12), the slow heat transport, and the high thermal capacity of the bulk sediment (Figure 5). A permanent GHSZ develops during the cold period (1963–2005) while gas hydrate is only intermittently stable when warm conditions prevail (1945–1962, 2008–2016). The base of the GHSZ (≥ thickness of GHSZ) is shifted to deeper sediment layers with increasing water depth due to the concurrent rise in hydrostatic pressure and decrease in geothermal heat flow (Table 2).

4. Discussion

New temperature measurements at five drill sites along a transect at the upper continental slope off Svalbard are used to constrain the geothermal gradients and thus the gas hydrate stability dynamics. Data from earlier heat-probe measurements within the upper 5–6 mbsf (Berndt et al., 2014) were unable to reach depths of equilibrated temperature conditions in the subsurface, induced by strong seasonal variation of bottom water temperatures. Our new temperature data from depths of up to 28 m are also affected by temperature fluctuations, but from a longer-term, decadal variability (Ferré et al., 2012). Yet these new data can still be used to back-calculate the background thermal gradients using a modeling approach. Our analyses shown here reveal higher geothermal gradients (and thus an overall thinner gas hydrate stability zone; GHSZ) than previously estimated by Berndt et al. (2014), who used regional heat flow values of ~50 mW/m^2, thermal conductivity values of the bulk sediments ranging from 1.5 to 2.4 Wm^{-1}K^{-1}, and thus yielding geothermal gradients ranging from 28 to

Figure 10. Results of the thermal modeling for site GeoB21632 for a geothermal heat flux of 108 mW·m^{-2} applied at 100 m sediment depth. The dashed line indicates the steady state profile for T_{BW} = 3°C applied as initial condition while the solid line depicts the results obtained at the end of the model period (year 2016). Dots indicate the measurements obtained in August 2016.

Figure 11. Sediment temperature (T), hydrostatic pressure (P_{HySt}, broken line), methane hydrate dissociation pressure (P_{Diss}, solid line), and gas hydrate stability zone (GHSZ, gray area where $P_{HySt} > P_{Diss}$) at site GeoB21632 as calculated for the year 2000.

33°C km^{-1}. In contrast, Thatcher et al. (2013) applied a regional (initial) heat flow value of 78.65 mW/m^2 and a geothermal gradient of 65°C km^{-1} (using seismic observations of a bottom simulating reflector as basic constraint) but on average much lower sediment thermal conductivity values (~1.2 Wm^{-1}K^{-1}) assuming a mostly clay-dominated sedimentary environment.

The method of temperature measurements with MeBo is based on employing MTLs, which is robust and simple to implement with the MeBo drill rig (Kopf et al., 2012). The MTL is inserted into the sediments and temperatures are measured for ~10 minutes allowing in most cases full equilibration of the probe to ambient temperatures. Uncertainties in the determination of the geothermal gradients are mostly from assumed depth of the measurements (within an interval of 25 cm) and overall sparse measurement intervals. Here, the most limiting factor is the overall penetration depth reached with MeBo. Due to the high abundance of glacial dropstones and highly lithified carbonate layers (Bohrmann et al., 2017), drilling was repeatedly abandoned and new holes had to be drilled for the same site. However, the combined data set of temperature values obtained off Svalbard points toward an average thermal gradient of 38 – 41°C km^{-1}. The consistency in temperature record obtained between the various drill sites suggests that the new temperature constraints are robust and we used them subsequently for modeling the dynamic evolution of the gas hydrate system. Porosity values obtained from the cored sediments have a considerable uncertainty (5–10%) due to the method used. However, the conversion from porosity to thermal conductivity is constrained by numerous in situ thermal conductivity measurements from previous heat-probe deployments and thermal conductivities are therefore reasonably well determined at all depths. For the modeling we use an exponentially decreasing best fit to the scattered porosity data (Figure 5a) ignoring the fast changing variability of the glacially-dominated sediment succession. This best-fit decrease in porosity was then turned into depth-dependent functions of thermal conductivity and heat capacity. Although this approach ignores changes in lithology over the considered depth range of 100 mbsf, adding more complex geology would not significantly alter the general outcome and conclusions of our study as the average physical properties would not be changed.
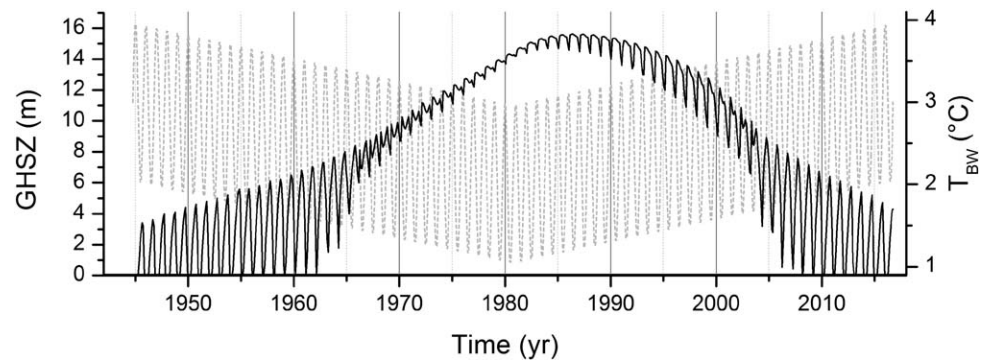
Figure 12. Thickness of the gas hydrate stability zone (GHSZ, solid line) at site GeoB21632. Bottom water temperature applied as model forcing is shown for reference (T_{BW}, gray dotted line, Figure 6).

Modeling of the dynamic response of the gas hydrate system over the past 70 years relies on the applied boundary conditions and temperature-forcing. Bottom water temperature changes (Ferré et al. 2012) suggest a ~2°C bottom water temperature decrease from 1945 until 1980, followed by an increase in temperature by about the same amount until 2016. In contrast, Westbrook et al. (2009) derived a temperature rise of only 1°C for the last three decades. On top of this long-term temperature change there is a strong seasonal variability of about ±2°C (Berndt et al., 2014). For numerical ease and overall simplicity, we have combined and simplified both trends with a mono-chromatic seasonal variation on top of a V-shaped long-term temperature trend (Figure 6). As this model ignores any previous changes to the temperature regime, it forces the initial boundary condition to be in equilibrium with the starting temperature of 3°C at the seafloor and the applied uniform thermal gradients at each modeled site. Any variation prior to 1945 and "memory" within the sediment column of previous thermal disturbance is ignored. Therefore, the detailed variation of the evolution in the thickness of the GHSZ is (especially for the initial decade) only to be seen as a conceptual model. The model of the current (August 2016) thickness and horizontal extent of the sI GHSZ superimposed on the seismic image (Figure 2) should be considered as a theoretical or potential zone of gas hydrate occurrence. In general, the sulfate-methane transition zone above which no gas hydrate can exist has a depth of 5–6 mbsf along the drilling transect visited during cruise MSM57 (Bohrmann et al., 2017). Therefore, the reported possible maximum vertical extent of the sI stability zone of ~4.5 m in August 2016 at Site GeoB21632 and GeoB21639 would generally not be occupied by gas hydrate. However, this does not exclude the possibility of shallow gas hydrate occurrence at localized gas seeps where focused gas advection overcomes the downward diffusion of sulfate (Graves et al., 2017).

The initial hypothesis by Westbrook et al. (2009) of gas hydrate dissociation induced by bottom water warming seems unlikely to explain the observations and temperature records obtained with MeBo70. Gas venting has been repeatedly seen at the same locations with the same extent along the margin throughout numerous expeditions to the region since the initial observation in 2009 and was again confirmed during MSM57 (Bohrmann et al., 2017). However, strong seasonal and decadal fluctuations have shifted the GHSZ multiple times across the study region laterally and vertically (Berndt et al., 2014). In principle, this would have resulted in repeated cycles of local gas hydrate formation followed by dissociation (Figure 12), and thus a lateral shift of gas venting if such venting were solely a result of gas hydrate dissociation. The steady location of gas venting thus seems to be controlled by other factors or processes, e.g., structurally confined gas transport along certain sedimentary layers (e.g., Chabert et al., 2011; Rajan et al., 2012; Sarkar et al., 2012), or possibly by tectonic features as proposed by Mau et al. (2017).

5. Conclusion

We present the first deep in situ temperature measurements conducted with the seafloor drill rig MARUM MeBo-70 from the upper slope of the Svalbard continental margin. Drilling was performed along a transect of five sites to investigate the dynamics of the gas hydrate system and associated gas migration. Measured temperatures suggest thermal gradients that vary from 38°C km^{-1} to 41°C km^{-1}, with temperature gradients decreasing slightly with increasing water depth. Measured porosities and calculated thermal

conductivities are used to model the thermal conditions at these sites to define the extent of the gas hydrate stability zone. The data show that only at water depths exceeding ~390 m, favorable theoretical sub-seafloor conditions existed for gas hydrate to form during the time of sampling in August 2016. At the drill site in 446 m water depth, the base of gas hydrate stability is estimated at ~60 m below seafloor. All other sites were outside the gas hydrate stability regime in August 2016. Strong seasonal and decadal temperature oscillations have a profound impact on the extent of the gas hydrate stability zone. Within a single year the maximum vertical extent is found during summer months when bottom water temperatures are low. Over the 70 year time period considered here (1945–2016), the maximum gas hydrate extent was determined from 1985 to 1990, after a 30 year steady decline in average bottom water temperatures. Since the minimum in bottom water temperatures in 1980, the extent of the gas hydrate stability zone is declining, and the location of flare sites should shift slowly down-slope. If such a shift cannot be documented by future repeat surveys it is likely that the flare locations are geologically controlled.

References

Berndt, C., Feseker, T., Treude, T., Krastel, S., Liebetrau, V., Niemann, H., et al. (2014). Temporal constraints on hydrate-controlled methane seepage off Svalbard. *Science*, *343* (6168), 284–287. https://doi.org/10.1126/science.1246298

Bohrmann, G., Ahrlich, F., Bergenthal, M., Bünz, S., Düßmann, R., Ferreira, C., et al. (2017). *R/V MARIA S. MERIAN Cruise Report MSM57, Gas Hydrate Dynamics at the Continental Margin of Svalbard* (204 p.). Bremen, Germany: MARUM – Zentrum für Marine Umweltwissenschaften, Fachbereich Geowissenschaften, Universität Bremen. ISSN 2195–7894.

Castelli, V., Stanley, E., & Fischer, E. (1974). The thermal conductivity of seawater as a function of pressure and temperature. *Deep Sea Research and Oceanographic Abstracts*, *21*(4), 1974) 311–319.

Chabert, A., Minshull, T. A., Westbrook, G. K., Berndt, C., Thatcher, K. E., & Sarkar, S. (2011). Characterization of a stratigraphically constrained gas hydrate system along the western continental margin of Svalbard from ocean bottom seismometer data. *Journal of Geophysical Research*, *116*, B12102. https://doi.org/10.1029/2011JB008211

Eldholm, O., Thiede, J., & Taylor, E. (1987). Evolution of the Norwegian continental margin: Background and objectives. In O. Eldholm, J. Thiede, E. Taylor, et al. (Eds.), Proceedings of Ocean Drilling Program, Initial Reports (Vol 104, pp. 5–25). College Station, TX: Ocean Drilling Program.

Faleide, J. I., Solheim, A., Fiedler, A., Hjelstuen, B. O., Andersen, E. S., & Vanneste, K. (1996). Late Cenozoic evolution of the western Barents Sea-Svalbard continental margin. *Global and Planetary Change*, *12*(1–4), 53–74. https://doi.org/10.1016/0921-8181(95)00012-7

Ferré, B., Mienert, J., & Feseker, T. (2012). Ocean temperature variability for the past 60 years on the Norwegian-Svalbard margin influences gas hydrate stability on human time scales. *Journal of Geophysical Research*, *117*, C10017. https://doi.org/10.1029/2012JC008300

Freudenthal, T., & Wefer, G. (2013). Drilling cores on the sea floor with the remote-controlled sea floor drilling rig MeBo. *Geoscientific Instrumentation, Methods and Data Systems*, *2*(2), 329–337. https://doi.org/10.5194/gi-2-329-2013

Graves, C. A., James, R. H., Sapart, C. J., Stott, A. W., Wright, I. C., Berndt, C., et al, (2017). Methane in shallow subsurface sediments as the landward limit of the gas hydrate stability zone offshore western Svalbard. *Geochimica et Cosmochimica Acta*, *198*, 419–438.

Hautala, S. L., Solomon, E. A., Johnson, H. P., Harris, R. N., & Miller, U. K. (2014). Dissociation of Cascadia margin gas hydrates in response to contemporary ocean warming. *Geophysicl Research Letters*, *41*, 8486–8494. https://doi.org/10.1002/2014GL061606

Huetter, E. S., Koemle, N. I., Kargl, G., & Kaufmann, E. (2008). Determination oft he effective thermal conductivity of granular materials under varying pressure conditions. *Journal of Geophysical Research*, *113*, E12004. https://doi.org/10.1029/2008JE003085

Intergovernmental Panel on Climate Change (2007). *Climate change 2007: The physical science basis: Working group I contribution to the fourth assessment report of the intergovernmental panel on climate change*. Cambridge, UK: Cambridge University Press.

Johnson, H. P., Miller, U. K., Salmi, M. S., & Solomon, E. A. (2015). Analysis of bubble plume distributions to evaluate methane hydrate decomposition on the continental slope. *Geochemistry, Geophysics, Geosystems*, *16*, 3825–3839. https://doi.org/10.1002/2015GC005955

Kennett, J. P., Cannariato, K. G., Hendy, I. L., & Behl, R. J. (2003). *Methane hydrates in quaternary climate change: the clathrate gun hypothesis*. Washington, DC: American Geophysical Union. ISBN 0–87590-296-0.

Ker, S., Le Gonidec, Y., Marsset, B., Westbrook, G. K., Gibert, D., & Minshull, T. A. (2014). Fine-scale gas distribution in marine sediments assessed from deep-towed seismic data. *Geophysical Journal International*, *196*(3), 1466–1470. https://doi.org/10.1093/gji/ggt497

Knies, J., Matthiessen, J., Vogt, C., Laberg, J. S., Hjelstuen, B. O., Smelror, M., et al. (2009). The Plio-Pleistocene glaciation of the Barents Sea–Svalbard region: a new model based on revised chronostratigraphy. *Quaternary Science Reviews*, *28*(9–10), 812–829. https://doi.org/10.1016/j.quascirev.2008.12.002

Kopf, A., Asshoff, K., Belke-Brea, M., Bergenthal, M., Bohrmann, G., Bräunig, A., et al. (2012). *Report and preliminary results of R/V SONNE cruise SO222. MEMO: MeBo drilling and in situ Long-term Monitoring in the Nankai Trough accretionary complex, Japan* (121 pp.). Bremen, Germany: Berichte, MARUM – Zentrum für Marine Umweltwissenschaften, Fachbereich Geowissenschaften, Universität Bremen. ISSN 2195–9633.

Landvik, J. O. N. Y., Bondevik, S. T. E. I. N., Elverhøi, A. N. D. E. R. S., Fjeldskaar, W. I. L. L. Y., Mangerud, J. A. N., Salvigsen, O. T. T. O., et al. (1998). The last glacial maximum of Svalbard and the Barents Sea area: ice sheet extent and configuration. *Quaternary Science Reviews*, *17*(1–3), 43–75. https://doi.org/10.1016/S0277-3791(97)00066-8

Landvik, J. Y., Ingólfsson, Ó., Mienert, J., Lehman, S. J., Solheim, A., Elverhøi, A., & Ottesen, D. A. G. (2005). Rethinking Late Weichselian ice-sheet dynamics in coastal NW Svalbard. *Boreas*, *34*(1), 7–24. https://doi.org/10.1111/j.1502-3885.2005.tb01001.x

Mau, S., Römer, M., Torres, M. E., Bussmann, I., Pape, T., Damm, E., et al. (2017). Widespread methane seepage along the continental margin off Svalbard - from Bjørnøya to Kongsfjorden. *Scientific Reports*, *7*, 42997. https://doi.org/10.1038/srep42997

Phrampus, B. J., & Hornbach, M. J. (2012). Recent changes to the Gulf Stream causing widespread gas hydrate destabilization. *Nature*, *490*(7421), 527–530. https://doi.org/10.1038/nature11528

Phrampus, B. J., Hornbach, M. J., Ruppel, C. D., & Hart, P. E. (2014). Widespread gas hydrate instability on the upper U.S. Beaufort margin. *Journal of Geophysical Research: Solid Earth*, *119*, 8594–8609. https://doi.org/10.1002/2014JB011290

Plaza-Faverola, A., Vadakkepuliyambatta, S., Hong, W.-L., Mienert, J., Bünz, S., Chand, S., & Greinert, J. (2017). Bottom-simulating reflector dynamics at Arctic thermogenic gas provinces: An example from Vestnesa Ridge, offshore west Svalbard. *Journal of Geophysical Research: Solid Earth*, *122*, 4089–4105. https://doi.org/10.1002/2016JB013761

Rajan, A., Mienert, J., & Bünz, S. (2012). Acoustic evidence for a gas migration and release system in Arctic glaciated continental margins offshore NW-Svalbard. *Journal of Marine and Petroleum Geology*, *32*(1), 36–49. https://doi.org/10.1016/j.marpetgeo.2011.12.008

Ruppel, C. D., & Kessler, J. D. (2017). The interaction of climate change and methane hydrates. *Reviews of Geophysics*, *55*, 126–168. https://doi.org/10.1002/2016RG000534

Sahling, H., Römer, M., Pape, T., Bergès, B., dos Santos Fereirra, C., Boelmann, J., et al. (2014). Gas emissions at the continental margin west of Svalbard: mapping, sampling, and quantification. *Biogeosciences*, *11*(21), 6029–6046. https://doi.org/10.5194/bg-11-6029-2014

Sarkar, S., Berndt, C., Minshull, T. A., Westbrook, G. K., Klaeschen, D., Masson, D. G., et al. (2012). Seismic evidence for shallow gas-escape features associated with a retreating gas hydrate zone offshore west Svalbard. *Journal of Geophysical Research*, *117*, B09102. https://doi.org/10.1029/2011JB009126

Solheim, A., Faleide, J. I., Andersen, E. S., Elverhøi, A., Forsberg, C. F., Vanneste, K., et al. (1998). Late cenozoic seismic stratigraphy and glacial geological development of the East Greenland and Svalbard—Barents Sea Continental Margins. *Quaternary Science Reviews*, *17*, 155–184.

Sharqway, M. H., Lienhard, J. H., & Zubair, S. M. (2010). Thermophysical properties of seawater: a review of existing correlations and data. *Desalination and Water Treatment*, *16*, 354–380. https://doi.org/10.5004/dwt.2010.1079

Thatcher, K. E., Westbrook, G. K., Sarkar, S., & Minshull, T. A. (2013). Methane release from warming induced hydrate dissociation in the West Svalbard continental margin. *Journal of Geophysical Research: Solid Earth*, *118*, 22–38. https://doi.org/10.1029/2012JB009605

Tishchenko, P., Hensen, C., Wallmann, K., & Wong, C. S. (2005). Calculation of the stability and solubility of methane hydrate in seawater. *Chemical Geology*, *219*(1–4), 37–52.

Vanneste, M., Berndt, C., Sverre Laberg, J., & Mienert, J. (2007). On the origin of large shelf embayments on glaciated margins—effects of lateral ice flux variations and glacio-dynamics west of Svalbard. *Quaternary Science Reviews*, *26*(19–21), 2406–2419. https://doi.org/10.1016/j.quascirev.2007.05.005

Vanneste, M., Guidard, S., & Mienert, J. (2005). Bottom-simulating reflections and geothermal gradients across the western Svalbard margin. *Terra Nova*, *17*(6), 510–516. https://doi.org/10.1111/j.1365-3121.2005.00643.x

Wallmann, K., Riedel, M., Hong, W. L., Patton, H., Hubbard, A., Pape, T., et al. (2018). Gas Hydrate dissociation at the continental margin off Svalbard induced by isostatic rebound rather than global warming. *Nature Communications*, *9*(1). https://doi.org/10.1038/s41467-017-02550-9

Westbrook, G. K., Thatcher, K. E., Rohling, E. J., Piotrowski, A. M., Pälike, H., Osborne, A. H., et al. (2009). Escape of methane gas from the seabed along the West Spitsbergen continental margin. *Geophysical Research Letters*, *36*, L15608. https://doi.org/10.1029/2009GL039191

Woodside, W., & Messmer, J. H. (1961). Thermal conductivity of porous media: I. Unconsolidated sands. *Journal of Applied Physics*, *32*(9), 1688–1699.